IOP Publishing
2D Mater. 12 (2025) 025001
https://doi.org/10.1088/2053-1583/ada040

2D Materials

CrossMark

OPEN ACCESS

RECEIVED
30 September 2024

REVISED
11 November 2024

ACCEPTED FOR PUBLICATION
17 December 2024

PUBLISHED
6 January 2025

PAPER

Room-temperature in-plane ferromagnetism in Co-substituted Fe_5GeTe_2 investigated by magnetic x-ray spectroscopy and microscopy

Emily Heppell[1,2,3,9], Ryuji Fujita[1,9], Gautam Gurung[1,4], Jheng-Cyuan Lin[1], Andrew F May[5], Michael Foerster[6], M Waqas Khaliq[6], Miguel Angel Niño[6], Manuel Valvidares[6], Javier Herrero-Martín[6], Pierluigi Gargiani[6], Kenji Watanabe[7], Takashi Taniguchi[8], Dirk Backes[2,*], Gerrit van der Laan[2,*] and Thorsten Hesjedal[1,2,*]

[1] Clarendon Laboratory, Department of Physics, University of Oxford, Parks Road, Oxford OX1 3PU, United Kingdom
[2] Diamond Light Source, Harwell Science and Innovation Campus, Didcot, Oxfordshire OX11 0DE, United Kingdom
[3] STFC, ISIS, Rutherford Appleton Laboratory, Didcot OX11 0QX, United Kingdom
[4] Trinity College, University of Oxford, Oxford OX1 3BH, United Kingdom
[5] Materials Science and Technology Division, Oak Ridge National Laboratory, Oak Ridge, TN 37831, United States of America
[6] ALBA Synchrotron, Carrer de la Llum 2-26, 08290 Cerdanyola del Vallès, Barcelona, Spain
[7] Research Center for Electronic and Optical Materials, National Institute for Materials Science, 1-1 Namiki, Tsukuba 305-0044, Japan
[8] Research Center for Materials Nanoarchitectonics, National Institute for Materials Science, 1-1 Namiki, Tsukuba 305-0044, Japan
[*] Authors to whom any correspondence should be addressed.
[9] These authors contributed equally.

E-mail: Dirk.Backes@diamond.ac.uk, Gerrit.vanderLaan@diamond.ac.uk and Thorsten.Hesjedal@physics.ox.ac.uk

Keywords: 2D van der Waals magnets, $(Co_{0.28}Fe_{0.72})_5GeTe_2$, ferromagnetism, x-ray absorption spectroscopy, x-ray magnetic circular dichroism, XPEEM

Supplementary material for this article is available online

Abstract

The exploration of two-dimensional (2D) van der Waals ferromagnets has revealed intriguing magnetic properties with significant potential for spintronics applications. In this study, we examine the magnetic properties of Co-doped Fe_5GeTe_2 using x-ray photoemission electron microscopy (XPEEM) and x-ray magnetic circular dichroism (XMCD), complemented by density functional theory calculations. Our XPEEM measurements reveal that the Curie temperature (T_C) of a bilayer of $(Co_xFe_{1-x})_{5-\delta}GeTe_2$ (with $x = 0.28$) reaches ~300 K—a notable enhancement over most 2D ferromagnets in the ultrathin limit. Interestingly, the T_C shows only a small dependence on film thickness (bulk $T_C \approx 340$ K), in line with the observed in-plane (IP) magnetic anisotropy and robust IP exchange coupling. XMCD measurements indicate that the spin moments for both Fe and Co are significantly reduced compared to the theoretical values. These insights highlight the potential of Co-doped Fe_5GeTe_2 for stable, high-temperature ferromagnetic applications in 2D materials.

1. Introduction

The discovery and exploration of two-dimensional (2D) materials have sparked significant interest due to their unique electronic, optical, and magnetic properties, which differ markedly from their bulk counterparts [1–4]. Among these, van der Waals (vdW) ferromagnets have emerged as a particularly exciting class of materials [5, 6] for potential applications in spintronics and data storage [7, 8], due to their ability to retain magnetic order down to monolayer thicknesses [9, 10], and their ease of integration into functional heterostructures [11–13]. Fe_3GeTe_2 was one of the first materials in which a persistent long-range magnetic order down to the monolayer limit was demonstrated, possessing a large perpendicular magnetic anisotropy and a high Curie temperature, T_C, of 230 K in the bulk [14] and 130 K in the monolayer limit [15]. The recently discovered 2D vdW ferromagnets, Fe_5GeTe_2 and Fe_3GaTe_2, have

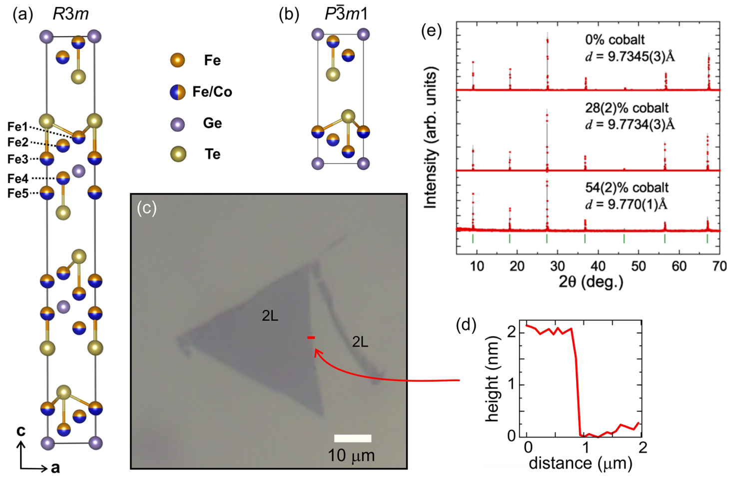

Figure 1. Crystal structure and optical micrograph of bilayer flake. Crystal structure of $(Co_xFe_{1-x})_5GeTe_2$ in the (a) $R3m$ and (b) $P\bar{3}m1$ space group. The Fe_5GeTe_2 monolayer has five Fe-containing Fe layers (termed Fe1–Fe5), while the Te atoms are located in the two outermost layers and the Ge layer is in the middle of the stack [19, 20]. The purple and golden spheres represent Ge and Te atoms, and the blue-bronze ones Fe or Co atoms (partial occupation) on Fe1, Fe2, Fe3, Fe4 and Fe5 sites, respectively. Note that for the common $R\bar{3}m$ space group of $(Co_xFe_{1-x})_5GeTe_2$, Fe1 is a split site, i.e. it can occupy up or down positions relative to Ge. Here, we only consider Fe1 in the up position, making the structure belong to the $R3m$ space group instead. The Fe1–Te and Fe4–Ge bonds form buckled hexagonal structures akin to graphene. The two are shifted by 1/3 of a diagonal unit cell vector with respect to each other. In contrast, Fe2, Fe3, and Fe5 are either above or below the hollow sites of these two layers [18, 27]. (c) Optical micrograph showing a triangular CoF5GT bilayer flake exfoliated on PDMS, which was investigated by XPEEM. The white scale bar has a length of 10 μm. (d) AFM linescan across the edge of the flake, as indicated in red, revealing a (homogeneous) bilayer thickness of ∼2 nm. (e) x-ray diffraction data (00l reflections) of the investigated 28% Co crystal (middle), along with an undoped (above) and a 54% Co crystal (below). Reprinted figure with permission from [27], Copyright (2020) by the American Physical Society.

attracted considerable attention owing to their room-temperature Curie temperatures and tunable magnetic properties, making them promising candidates for both fundamental research and practical applications [10, 16, 17].

Fe_5GeTe_2 exhibits ferromagnetic (FM) ordering with a T_C of ∼270–310 K, which is relatively high among 2D ferromagnets [18–20] and close to the rivaling class of doped semiconducting transition metal dichalcogenides (with a monolayer T_C of up to 360 K) [21]. This property opens the door to potential room-temperature applications [8, 22–25]. Furthermore, Fe_5GeTe_2 displays magnetic anisotropy and a layered structure, enabling the exfoliation of few-layer and monolayer samples while maintaining its FM properties [18, 26]. However, the magnetic properties of Fe_5GeTe_2 can be further enhanced and tailored through chemical doping, which introduces additional degrees of freedom in tuning its electronic and magnetic behavior [27–29].

The substitution of Co atoms for Fe in the Fe_5GeTe_2 lattice is influencing the exchange interactions and the density of states near the Fermi level, thereby altering its magnetic characteristics. In fact, $(Co,Fe)_5GeTe_2$ hosts both FM and antiferromagnetic (AF) order depending on the degree of Co substitution, whereby a critical Co concentration of 0.4 has been reported, above which AF order emerges [27, 28]. Moreover, for a concentration of 0.44, FM and AF order coexist at room temperature with odd-layer FM in the monolayer limit [30]. However, owing to the richness of the magnetic phenomena in this material, the magnetic ground state is complex, and so far, element-specific resonant magnetic x-ray scattering had only been carried out in the AF state [29].

The properties of the parent compound Fe_5GeTe_2, which crystallizes in the rhombohedral space group $R\bar{3}m$, are governed by Fe vacancies and the thermal cycling history [31], mostly affecting the Fe1 site (see figure 1(a)). As the exact stoichiometry can differ, Fe_5GeTe_2 is generally referred to as $Fe_{5-\delta}GeTe_2$. Note that $(Co_xFe_{1-x})_{5-\delta}GeTe_2$ with $x < 0.4$ crystallizes, in principle, in the same space group [18]. However, due to the large density of stacking faults, there is likely significant mixing of the primitive AA and rhombohedral ABC stacking orders in these Co-substituted bulk crystals [32] (compare figures 1(a) and (b)).

Here, we present an investigation of the magnetic properties of the FM 2D material $(Co_xFe_{1-x})_{5-\delta}GeTe_2$ (with $x = 0.28$; CoF5GT thereafter) using a combination of element-specific, x-ray-based magnetic spectroscopy and microscopy, supported by theoretical calculations. We aim to elucidate how Co doping affects the Curie temperature, magnetic anisotropy, and coercive field of Fe_5GeTe_2. Understanding these changes is crucial for optimizing the material for various technological applications.

2. Materials and methods

2.1. Co-doped Fe_5GeTe_2 sample preparation

The CoF5GT bulk single crystals were synthesized via an iodine-assisted chemical vapor transport technique, and structurally, chemically and magnetically characterized in detail using x-ray diffraction, energy-dispersive spectroscopy (EDS) and SQUID magnetometry, respectively, as previously discussed in [27]. For magnetic spectroscopy, bulk crystals were cleaved in an Ar-filled glovebox connected to the synchrotron end station. For the magnetic x-ray microscopy study, ultrathin layers of CoF5GT were exfoliated with a polymethyldisiloxane (PDMS)-assisted technique in an Ar-filled glovebox, and encapsulated between thin layers of hBN to prevent oxidation.

Figure 1(c) shows an optical micrograph of the bilayer (2L) CoF5GT flake exfoliated over PDMS. The flake thickness was determined via atomic force microscopy (AFM), as shown in figure 1(d), scanning across a step-edge. Figure 1(e) displays x-ray diffraction data (00*l* reflections) comparing the $x = 0.28$ Co-substituted sample (which is the focus of this study) with undoped Fe_5GeTe_2 and a sample with a very high Co concentration ($x = 0.54$), revealing the structural influence of Co substitution. The Co concentration was determined by EDS to be $x = 0.28$ [27]. The results of the structural study are discussed in detail in [27] and can be briefly summarized as follows: First, the $x = 0.28$ crystal is strongly affected by stacking disorder, preventing a refinement of the structure. In contrast, for the $x = 0.54$ sample, stacking faults present no issue for the refinement, yielding space group $P\bar{3}m1$. Second, Co incorporation leads to a slight contraction in the *ab* plane, along with an increase in both the slab thickness and interlayer spacing.

2.2. Magnetic domain imaging with x-ray photoemission electron microscopy (XPEEM)

XPEEM measurements were conducted at the BL24-CIRCE beamline at the ALBA Synchrotron in Barcelona, Spain [33]. Real-space imaging was conducted at the Fe L_3 (706.2 eV) and Co L_3 (769.0 eV) edges in the temperature range from 250 to 310 K [34]. The fixed angle of incidence of the incident x-rays with respect to the sample surface was 16°, which means that 28% of the sample's out-of-plane (OOP) magnetization component is projected along the x-ray propagation direction [35, 36]. Here, the x-ray magnetic circular dichroism (XMCD) asymmetry is defined as $(\mu^-_{\rm max} - \mu^+_{\rm max})/(\mu^-_{\rm max} + \mu^+_{\rm max})$, where $\mu^-_{\rm max}$ and $\mu^+_{\rm max}$ are the XAS signals at the maximum difference taken with left and right circularly polarized x-rays, respectively.

2.3. Magnetic x-ray spectroscopy

X-ray absorption spectroscopy and magnetic circular dichroism measurements were conducted at the HECTOR end station on beamline 29 (BOREAS) at the ALBA Synchrotron [37]. XAS spectra across the Fe (695–745 eV), Co (765–810 eV), and Ge (1200–1290 eV) $L_{2,3}$, as well as the Te $M_{4,5}$ (565–595 eV) edges were recorded using right- and left-circularly polarized (RCP and LCP) x-rays at normal incidence (NI), with a magnetic field of up to 6 T applied along the beam direction. The XAS signal, $I_{\rm sum}$, is defined as $I_{\rm sum} = \mu^- + \mu^+$, while the XMCD signal is defined as $I_{\rm xmcd} = \mu^- - \mu^+$ [38]. The measurements were performed in total-electron yield detection mode, sensitive to the upper 3–5 nm of the sample [38], at a temperature of 10 K unless otherwise specified.

Spin and orbital magnetic moments for Fe and Co were determined using sum rule analysis [39]. Using the scale shown on the right-hand side of the panels in figures 3(c) and (d), the quantities $p = \int_{L_3} \mathrm{d}E\, I_{\rm xmcd}$ and $q = \int_{L_3,L_2} \mathrm{d}E\, I_{\rm xmcd}$ can be determined, and from figures 3(e) and (f), the quantity $r = \int_{L_3,L_2} \mathrm{d}E\, I_{\rm sum}$. Accounting for the number of holes in the 3*d* shell $n_h = 10 - n_d$, which is assumed to be 4 for Fe^{2+} and 3 for Co^{2+}, the spin and orbital moments per Fe and Co atom were obtained as $m_{\rm orb} = -\langle L_z \rangle = -(4/3)qn_h/r$ and $m_{\rm spin,eff} = -2\langle S_{{\rm eff},z}\rangle = -(6p - 4q)n_h/r$ [38]. Also $m_{\rm spin,eff} = m_{\rm spin} - 7\langle T_z \rangle$.

Note that experimental limitations of the sum rule analysis can arise in multiple ways [40], such as caused by saturation effects, *jj* mixing, continuum background corrections, canted spin moments, arbitrary integration limits, estimation of the hole number, omission of linear dichroism in sum spectrum, and neglect of the magnetic dipole term. All these effects, which on their own can either decrease or increase the moment value, are usually assumed to accumulate to a total error for Co and Fe of ∼10% [41].

2.4. Density functional theory (DFT) calculations

DFT calculations were performed using VASP [42]. We applied the generalized gradient approximation [43] using the projector augmented wave method [44]. Spin–orbit coupling was included in all the calculations. vdW interactions between the 2D layers were considered using DFT-D3 method with Becke–Johnson damping [45]. The bulk atomic structure of Fe_5GeTe_2 with space group $R\bar{3}m$ allows split sites for Fe1 (that can occupy up or down positions relative to Ge). In this work, we only considered a simple bulk structure with space group $R3m$ by fixing Fe1 in the up positions. We fixed the lattice parameters to the reported experimental values ($a = 4.04$ Å, $c = 29.25$ Å for $R3m$ [18] and $a = 4.02$ Å, $c = 9.8$ Å for $P\bar{3}m1$ [27]), and all atomic positions were relaxed using a $20 \times 20 \times 4$ Γ-centered *k*-point grid with a kinetic energy cutoff of 500 eV. For the supercell structure, a 11 × 11 × 2 Γ-centered k-point grid was used. The relaxation process was repeated until the atomic forces on each atom were less than 0.01 eV Å^{-1}. The doping effect in $(Co_xFe_{1-x})_5GeTe_2$ was simulated using the virtual crystal approximation (VCA), and, additionally, by constructing a $\sqrt{3} \times \sqrt{3} \times 1$ supercell to account for substitutional Co doping at Fe1 positions. Our previous DFT calculations suggest that the Fe1 site is the most favorable for Co doping [27]. Hole doping simulations were performed by reducing the total number of electrons via a compensating uniform background charge. The magnetic anisotropy was calculated using the magnetic force theorem with an electronic convergence of 10^{-8} eV. The plots in figure 1 were created using VESTA [46].

3. Results and discussion

3.1. XPEEM study of bilayer CoF5GT

XPEEM images of FM domains in bilayer CoF5GT were acquired as a function of temperature. The XPEEM image taken at 259 K (figure 2(a)) shows large, μm-sized domains (white or black contrast). As the magnetic contrast is governed by the easy plane character of CoF5GT (see magnetic spectroscopy results below), the magnetic moments within these black and white domains are oriented in-plane (IP) and in opposite directions to one another. In-between, smaller domains are found, which disappear first upon heating the sample to 282 K. A general loss of contrast is observed as the temperature is increased to 296 K and above, i.e. closer to T_C. However, the larger domains remain magnetic up to 302 K. No qualitative change of the magnetic contrast is observed as a function of temperature. From the loss of magnetic contrast, the CoF5GT bilayer T_C can be estimated to be ∼302 K (figure 2(d)), whereas the Co concentration-dependent bulk T_C was previously determined to be ∼340 K for this Co stoichiometry [27]. Compared to other 2D Ising ferromagnets, including Fe_3GeTe_2 [15] and $CrGeTe_3$ [10], the relatively high T_C of CoF5GT [47] appears to depend less significantly on the number of layers, suggesting a relatively weak intralayer exchange interaction. On the other hand, the high-T_C ferromagnetism in CoF5GT may be stabilized by intralayer exchange interactions confined within the unit cell.

To shed light on the microscopic origin of this behavior, we carried out XMCD measurements and DFT calculations, which are discussed in detail below.

3.2. Orbital and spin magnetic moments of bulk CoF5GT

The orbital and spin magnetic moments of the Fe and Co sites were obtained from sum rule analysis of the XAS and XMCD spectra [48, 49], measured in total electron yield detection mode. In figures 3(a), (c), (e) and (b), (d), (f), XAS and XMCD spectra of Fe and Co, respectively, are shown as measured at 10 K in an applied field of 6 T in grazing incidence (GI). The XAS spectra shown in figures 3(a) and (b) were taken with 100% RCP and LCP (labeled μ^+ and μ^- in the figure), and the respective XMCD spectra shown in the panels below calculated by subtracting them from each other (figure 3(c) and (d)). A step function with a ratio of 2:1 for the L_3 and L_2 edges, respectively, was subtracted from the XAS spectra to remove the continuum-state background before integration. The integrals p and q over the L_3 and $L_{2,3}$ edges, respectively, of the XMCD used for the sum rule analysis are indicated in figures 3(c) and (d). The integrated XAS intensity over the $L_{2,3}$ edges provides the normalization factor r (figures 3(e) and (f)). For further details, we refer to section S1.3.

In table 1, the results of the sum rule analysis are summarized. The spectra were taken at temperatures of 300 and 10 K and in an applied magnetic field of 6 T at both GI and NI to probe the IP and OOP components of the magnetization, respectively. (The measurement geometry is illustrated in figure 5(f)). At 6 T, $m_{\text{spin,eff}}$ reaches 2.5 μ_B atom^{-1} for Fe and 1.4 μ_B atom^{-1} for Co at 10 K, which is about 30% reduced at 300 K [in the case of Fe]. These values for the spin moments are not far out of line with those for bcc Fe (1.98 μ_B atom^{-1}) and hcp Co (1.62 μ_B atom^{-1}) [50]. Also, they are comparable with reports on undoped Fe_5GeTe_2 bulk crystals of $m_{\text{spin,eff}} = 1.8\ \mu_B$/Fe ($m_{\text{orb}} = 0.1\ \mu_B$/Fe, in general agreement with our findings) [51]. For a further discussion, see section S1.3.

Table 1 also lists the orbital moments, m_{orb}, and the ratio of orbital-to-spin moments, $m_{\text{orb}}/m_{\text{spin,eff}}$. We note that the absolute values of m_{orb} are larger for Fe in the NI geometry but larger for Co in the GI geometry, pointing towards differences in the magnetocrystalline anisotropy energies. This finding will be discussed in the context of the magnetic hysteresis loop measurements in the magnetic anisotropy section below. Further, the ratio $m_{\text{orb}}/m_{\text{spin,eff}}$ is a useful indicator of the importance of the orbital properties, as in this ratio, the number of holes and the varying saturation fields cancel out. According to Hund's third rule, the spin and orbital moments for the more-than-half-filled Fe and Co band are aligned parallel. Indeed, from the sum rule analysis, we find $m_{\text{orb}}/m_{\text{spin,eff}} > 0$ in both cases. The experimental values of the magnetic moments will be further discussed in the context of the DFT results below.

3.3. Magnetic spectroscopy at the Ge $L_{2,3}$ and Te $M_{4,5}$ edges

Apart from the element-selective analysis of the magnetic Fe and Co ions at their $L_{2,3}$ edges, giving XMCD signals which are proportional to their 3d magnetic

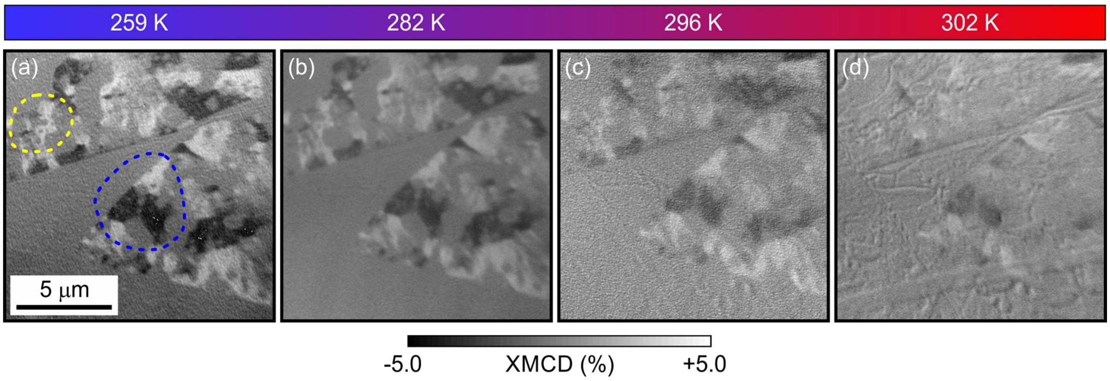

Figure 2. XPEEM measurements as a function of temperature. The magnetic contrast at (a) 259 K and (b) 282 K is dominated by larger, μm-sized domains. (c) At 296 K, the magnetic contrast is reduced, and at (d) 302 K, it has almost completely vanished, except for larger domains. Examples of both larger (blue) and smaller (yellow) domains are indicated in panel (a).

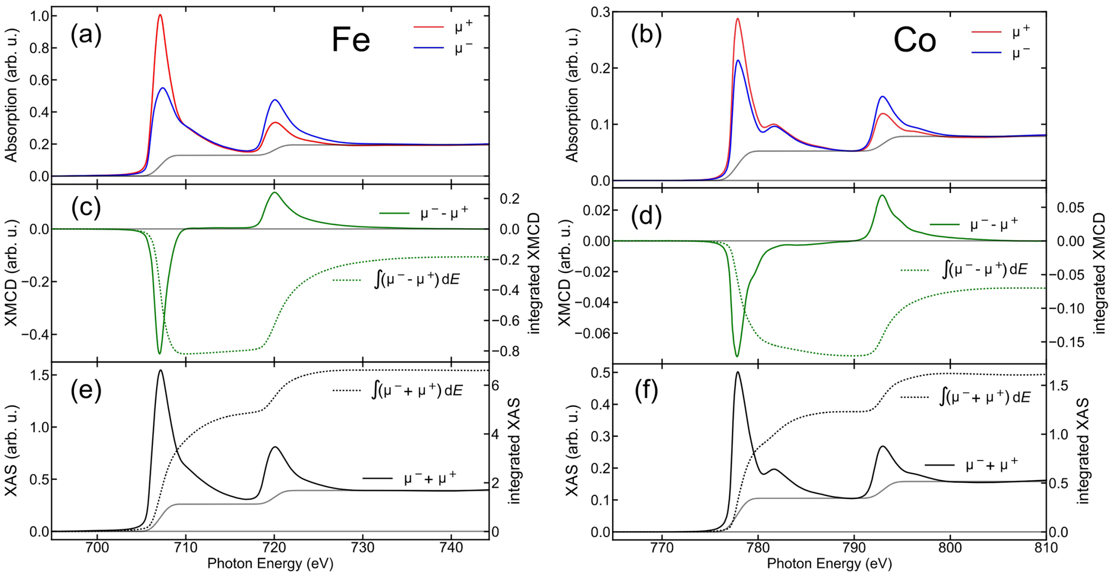

Figure 3. Right- (red, μ^+) and left- (blue, μ^-) circularly polarized (a), (b) XAS, (c), (d) XMCD (solid green line) and integrated XMCD (dotted green line), and (e), (f) summed (solid black line) and integrated (dotted black line) XAS spectra over the Fe $L_{2,3}$ (left column) and Co $L_{2,3}$ (right column) edges. The spectra were measured in total electron yield in grazing incidence at an angle of 20° (off the surface plane) at 10 K under a 6 T magnetic field applied along the same grazing incidence direction. The gray step function in (a), (e) and (b), (f) denotes the continuum-state background subtracted before integration.

Table 1. Results of the sum rule analysis for the measurements at 10 K, in an applied field of 6 T, for grazing and normal incidence (GI/NI). The magnetic moments $m_{\mathrm{spin,eff}}$ and m_{orb} are given in units of μ_B/Fe or Co atom. The number of holes was assumed to be $n_h = 4$ for Fe and $n_h = 3$ for Co. An error on the order of 10% can typically be assumed for the magnetic spin moments of Co and Fe [41].

Element	Geometry	m_{orb}	$m_{\mathrm{spin,eff}}$	$m_{\mathrm{orb}}/m_{\mathrm{spin,eff}}$
Fe	GI	0.148	2.45	0.0604
	NI	0.167	2.53	0.0661
Co	GI	0.174	1.39	0.125
	NI	0.135	1.25	0.108

moment, also the ‘non-magnetic’ elements Ge and Te can be analyzed. This is important since these elements can exhibit a net spin polarization through hybridization of their p bands with the $3d$ band of Fe or Co, giving an XMCD signal. Figures 4(a) and (b) show the Ge $L_{2,3}$ and Te $M_{4,5}$ edge XAS (top) and XMCD (bottom) spectra, respectively, measured at 10 K in an applied magnetic field of 6 T at GI. This observation of spin-polarized Ge and Te states in CoF5GT is consistent with their observation in undoped Fe_5GeTe_2 [51]. The sizeable Te-XMCD (observed in Fe_5GeTe_2) has been argued by Yamagami *et al* [51] to be hinting at the major role spin–orbit coupling of this heavy element could play in the arrangement of the Fe spins, including magnetocrystalline anisotropy, similar to the role of Pt in the itinerant ferromagnet FePt [52].

For Ge (for which the $3d$ shell should be fully occupied), the $L_{2,3}$ ($2p \rightarrow 3d$) edges are located at ~1240 eV. Here, the same XMCD sum rule analysis as for Fe and Co can be applied, using a step height ratio

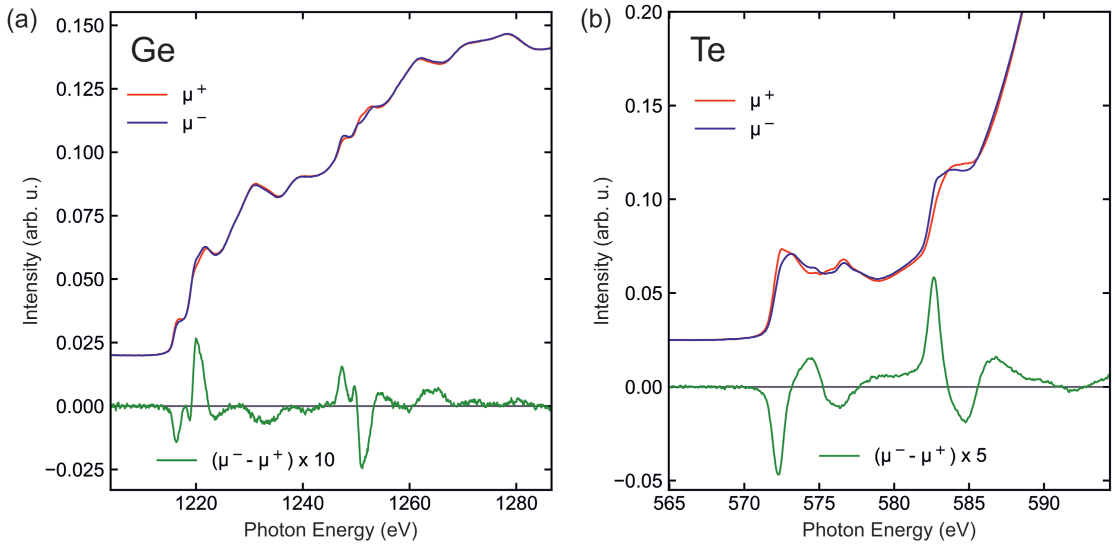

Figure 4. Right- (red, μ^+) and left- (blue, μ^-) circularly polarized XAS and XMCD (green) over the (a) Ge $L_{2,3}$ and (b) Te $M_{4,5}$ edges in total electron yield. The measurements were performed in grazing incidence (at 20° off the surface plane) at 10 K under a field of 6 T applied along the incident beam direction.

of L_3:$L_2 = 2$:1 in the XAS background correction. On the other hand, for Te with its $M_{4,5}$ edges at ∼570 eV, i.e. a $3d \rightarrow 5p$ transition, different coefficients for the XMCD sum rule are used [53]. Sum rule analysis gives at the M_4 edge, $I_{\mathrm{xmcd}}/I_{\mathrm{sum}} = 3/2\,\langle S_z\rangle/n_h$ and at the M_5 edge, $I_{\mathrm{xmcd}}/I_{\mathrm{sum}} = -\langle S_z\rangle/n_h$, where, as usual, the expectation value of the spin moment is defined as $m_{\mathrm{spin}} = -2\langle S_z\rangle$ and n_h is the number of holes [38]. The step height in the XAS background correction for M_5:M_4 is 3:2. Note that as the XMCD measures the moment on the 5p electrons, we can neglect the small orbital contribution for Te. Also, note that the Te $M_{4,5}$ absorption ($3d \rightarrow 5p$ transition) reverses the XMCD sign compared to the $p \rightarrow d$ transition ($L_{2,3}$). Therefore, since the Te M_5 and Fe L_3 XMCD have the same sign, the Te 5p and Fe 3d moments are aligned antiparallel.

As the Te spectra possess a sloping background that curls significantly at the M_4 edge and beyond, we focused on the M_5 edge for the sum rule analysis. Linear backgrounds fitted to the M_5 pre-edge were subtracted from the Te spectra. The height of the M_5 step for the XAS background correction was set to the lowest intensity of RCP and LCP between the M_5 and M_4 peaks (with respect to the pre-edge background). This way, from sum rule analysis for Te, spin moments of $m^{\mathrm{GI}}_{\mathrm{spin,eff}} = 2 \cdot I_{\mathrm{xmcd}}/I_{\mathrm{sum}} = 0.092\,\mu_{\mathrm{B}}$/hole and $m^{\mathrm{NI}}_{\mathrm{spin,eff}} = 0.113\,\mu_{\mathrm{B}}$/hole were determined from the GI and NI data at 10 K in a field of 6 T, respectively. The presence of a relatively large spin moment m_s per hole of $-0.092\,\mu_{\mathrm{B}}$ on the Te site is evidence of a significant intralayer hybridization between the Fe 3d and Te 5p orbitals in bulk CoF5GT. To reach agreement between the DFT calculations (see below) and our experimental value, ∼0.5 holes per Te have to be assumed, giving $m_s = -0.045\,\mu_{\mathrm{B}}$/Te atom, which confirms the strong hybridization between the metal 3d and Te 5p bands. Moreover, in the plot of the Fermi surfaces of Fe and Te (figure S1), we find a strong hybridization of the Fe and Te bands near the Γ point. This is further enhanced in Co-substituted Fe$_5$GeTe$_2$, as can be seen in the atom-projected density-of-states (DOS) plots in figure S3.

The unique temperature evolution of the magnetic properties of undoped (and doped) Fe$_5$GeTe$_2$ [18], which includes the appearance of non-collinear spin structures and ferrimagnetic behavior [54, 55], was explained by Yamagami *et al* [51] to be governed by the hybridization between the Fe1 site and Te. In terms of bond distance, Fe1 is the second closest to Te (2.61 Å), however, it forms a buckled hexagonal structure like graphene, while for the closest Fe site, Fe4 and Te are vertically stacked [20]. This bond configuration is absent in the closely related vdW magnet Fe$_3$GeTe$_2$, which has a much lower transition temperature.

3.4. Magnetic anisotropy

To determine the magnetic anisotropy of the sample, and to obtain unambiguous experimental proof of the hybridization between Te and Fe/Co states, we carried out measurements of the magnetic field dependence of the XMCD at 10 and 300 K. Figure 5 shows element-specific hysteresis loops for (a), (b) Fe, (c), (d) Co, and (e) Te in both NI and GI, with the measurement geometry illustrated in figure 5(f). Note that the Ge signal was too noisy to carry out measurements of the hysteresis loop (and so was the Te measurement at 300 K). All three loops at 10 K show qualitatively the same behavior, i.e. an OOP hard axis (measured at NI) and an IP easy axis (measured at GI) with a very small coercive field. Importantly, the

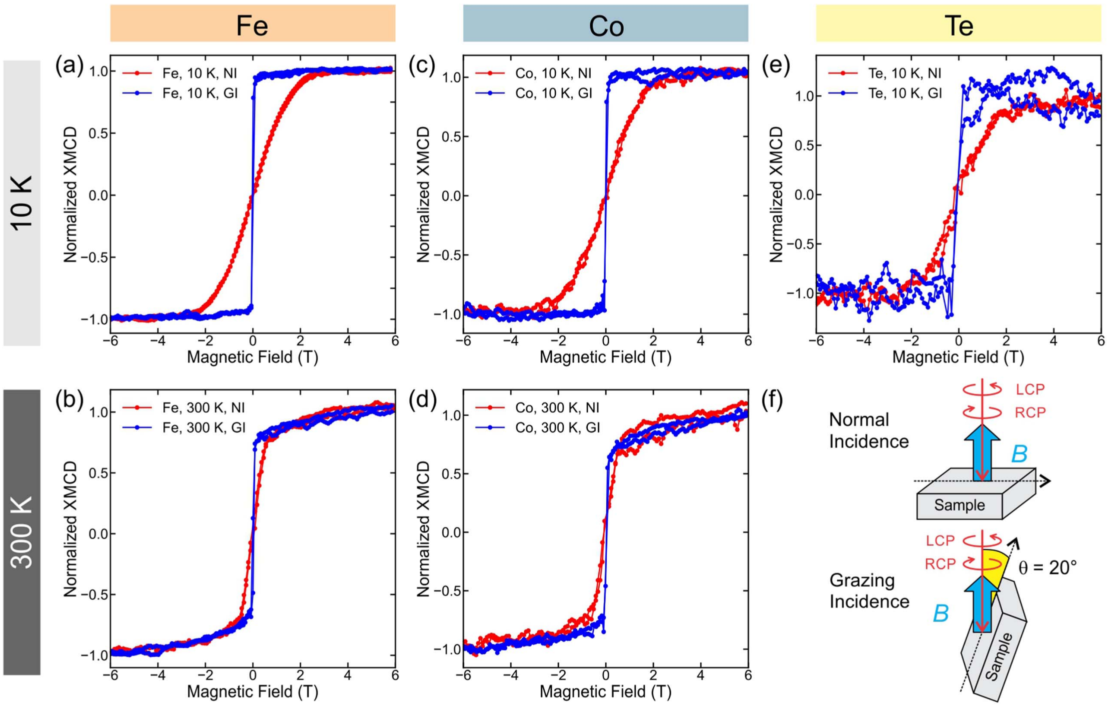

Figure 5. Element-specific magnetization curves of $(\mathrm{Co}_{0.28}\mathrm{Fe}_{0.72})_5\mathrm{GeTe}_2$ recorded at the (a), (b) Fe L_3 (703.8 eV off-edge / 706.9 eV on-edge), (c), (d) Co L_3 (774.2 eV off-edge / 777.75 eV on-edge), and (e) Te M_5 (569.9 eV off-edge / 572.2 eV on-edge) edges in total electron yield. The measurements were carried out in both normal (NI, red) and grazing incidence (GI = 20° off the horizon, blue) at (a), (c), (e) 10 K and (b), (d) 300 K. The curves have been normalized to their saturation values at high field. (f) Illustration of the normal and grazing incidence measurement geometries.

field-dependence of the (normalized) Fe, Co, and Te XMCD at 10 K is qualitatively identical, indicating their strong coupling. At 300 K, i.e. ~30 K below the bulk T_C, the anisotropy has markedly reduced with both the NI and GI loops for Fe and Co (figures 5(b) and (d)) showing a similar easy axis behavior. This is consistent with the intralayer exchange coupling being stronger than the interlayer coupling. Further, the magnetization does not seem to saturate at the maximum field of 6 T, pointing towards materials inhomogeneities and the existence of a paramagnetic background.

While the hysteresis curves in figure 5 clearly show for both Fe and Co at 10 and 300 K that the easy axis is IP (GI geometry), the sum rule analysis results in table 1 (measured at the maximum applied field of 6 T) seems more ambiguous at first glance. Using perturbation theory, Bruno proposed a model for the magnetocrystalline anisotropy energy (MAE) under the assumption that the majority spin band is completely filled [56]. Bruno's model states that the absolute value of the orbital moment is larger along the easy magnetization direction, and that the difference between the orbital moments along the easy and hard directions is proportional to the MAE. Comparing the orbital moments for Fe and Co (table 1), measured in GI and NI, one notes that for Fe [$\Delta\left(m_{\mathrm{orb}}^{\mathrm{GI}} - m_{\mathrm{orb}}^{\mathrm{NI}}\right) = -0.019\,\mu_{\mathrm{B}} < 0$] the MAE prefers a magnetization direction that is OOP, disagreeing with the hysteresis behavior, while for Co [$\Delta\left(m_{\mathrm{orb}}^{\mathrm{GI}} - m_{\mathrm{orb}}^{\mathrm{NI}}\right) = 0.039\,\mu_{\mathrm{B}} > 0$] the MAE prefers a magnetization direction that is IP, in agreement with the hysteresis.

To understand the opposite trend, one has to bear in mind that the hysteresis curves are predominantly determined by the behavior of the spin moment. Therefore, while the (local) orbital moment reflects the MAE of the ion, the spin moments are affected by the exchange interaction between them, making in this case Fe follow the IP behavior of Co. This 'magnetic bully' effect has been first demonstrated in ultrathin Co/Ni films, in which, using XMCD, it was found that the stronger anisotropy contribution of a much thinner Co layer redirects the easy magnetization direction of the entire film [57]. While for 3*d* transition metals, the orbital moment m_{orb} is assumed to be proportional to the MAE of the specific atom, the situation is completely different for the spin moment. Bruno [56] used second-order perturbation theory to derive the effect of the small orbital moment on the magnetocrystalline anisotropy, and this cannot be applied to the spin moment. Following [58], the spin moment is isotropic, so that $m_{\mathrm{spin}} = \left[m_{\mathrm{spin,eff}}^{\mathrm{OOP}} + 2m_{\mathrm{spin,eff}}^{\mathrm{IP}}\right]/3$, and the anisotropy in the measured effective spin moment is due to the magnetic dipole term $\langle T_z\rangle$. Using $m_{\mathrm{spin,eff}}^{\mathrm{OOP}} = m_{\mathrm{spin,eff}}^{\mathrm{NI}}$, and approximating $m_{\mathrm{spin,eff}}^{\mathrm{IP}}$ by $m_{\mathrm{spin,eff}}^{\mathrm{GI}}$, we obtain the following (absolute) values for $\langle T_z\rangle$: $-0.0076\,\mu_{\mathrm{B}}$ per Fe atom and $-0.0067\,\mu_{\mathrm{B}}$ per Co atom, which is ~0.5%

of m_{spin} for Co. The magnetic dipole term has no influence on the exchange interaction, but it gives a small contribution to the magnetic anisotropy (see equation (28) in [58]). This is because $\langle T_z \rangle$ accounts for a spin quadrupole moment [59] as well as for spin-flip excitations between the exchange split majority and minority spin bands. Furthermore, the Bruno model is strictly only valid if the minority band is completely empty [58], which is of course not really the case for the Fe and Co atoms. Thus, there are small additional terms besides the orbital moment anisotropy, which can be neglected in our case.

On the other hand, the hysteresis loops are dominated by the dichroism due to the spin moment, which is much larger than that of the orbital moment. As mentioned, the spin moment is isotropic and its absolute value is not expected to change as a function of applied field. However, below a certain field threshold, the spin moments, when measured along the hard axis, will tilt away towards the easy axis. Then, the projection of the spin moments onto the beam direction (which is taken along the field) becomes smaller, thereby reducing the dichroism signal. This explains the behavior of the magnetization loops in figure 5, and makes it a more direct indicator for the easy direction than the orbital moment values.

The observed IP magnetic anisotropy is in contrast with other vdW ferromagnets, such as CrI_3 and Fe_3GeTe_2, which typically exhibit OOP (perpendicular) magnetic anisotropy due to stronger spin–orbit coupling effects that stabilize perpendicular magnetic orientations. In Co-doped F5GT, however, Co substitution shifts the anisotropy to an IP configuration, a characteristic that enhances the magnetic stability within the atomic layers. This IP alignment is significant, as it improves the stability of magnetic order even in ultrathin layers, making this material particularly promising for spintronic applications that benefit from IP magnetization. This unique anisotropy in Co-doped F5GT demonstrates the potential to tune vdW materials to fit specific application needs through chemical doping.

3.5. DFT calculations

The magnetic anisotropy in $Fe_{5-\delta}GeTe_2$ bulk crystals depends on Fe vacancies, which introduce hole doping. In our DFT calculations for bulk Fe_5GeTe_2 (space group $R\bar{3}m$), we identified IP anisotropy with a value of 0.41 meV/f.u. and an average magnetic moment of 1.68 μ_B/Fe atom. Upon Co doping ($x = 0.25$) using the VCA, the anisotropy remained IP but reduced to 0.18 meV/f.u. The Fe (average) and Co moments were 1.75 and 1.97 μ_B atom^{-1}, respectively, though discrepancies with experimental XMCD values suggest that Fe vacancies and model simplicity might be influencing these results. Increased hole doping enhanced the magnetic moment by approximately 21% (see figure S1).

In the primitive $P\bar{3}m1$ unit cell, Fe_5GeTe_2 exhibited IP anisotropy (0.40 meV/f.u.), but Co doping ($x = 0.25$) switched the easy axis to OOP with 0.60 meV/f.u., contradicting experimental findings. Potential explanations include disorder, Fe1 site variations, or strain effects in 2D materials. We also explored the $\sqrt{3} \times \sqrt{3} \times 1$ supercell of the $R3m$ structure, motivated by the supercell observed in the x-ray diffraction data [27], which showed that Co doping reduces IP anisotropy and increases hybridization between Co $3d$ and Te $5p$ states (see section S5 for details and the results summarized in table S1). This behavior is consistent with the atom-projected DOS findings presented in figure S3.

4. Conclusion

In this study, we investigated the magnetic properties of Co-doped Fe_5GeTe_2 using a combination of XPEEM, XMCD measurements, and DFT calculations. Our XPEEM measurements reveal a remarkably high Curie temperature of ∼300 K for a bilayer of CoF5GT, which is significantly higher than that of other materials in that class of 2D ferromagnets in the ultrathin limit. Notably, the T_C shows only a small dependence on film thickness, consistent with the observed IP magnetic anisotropy and stronger IP exchange coupling. The XMCD measurements provided insights into the spin moments of Fe and Co, showing an increase and reduction, respectively, compared to theoretical predictions from DFT calculations. The XMCD measurements also highlighted the orbital moment anisotropy of the elemental constituents, demonstrating that the introduction of Co redirects the easy magnetization direction due to its preference for IP anisotropy. This finding is critical for the development of stable, high-temperature 2D ferromagnets and underscores the potential of chemical doping to tune the magnetic properties of 2D vdW ferromagnets.

Data availability statement

All data that support the findings of this study are included within the article (and any supplementary files).

Acknowledgments

The XMCD experiments were performed at the BOREAS beamline, and the XPEEM experiments at the CIRCE beamline, both at the ALBA Synchrotron under proposals 2023027573 and 2022097164, respectively. E H acknowledges a STFC-Diamond-EPSRC studentship (2604894, EP/R513295/1, EP/T517811/1). K W and T T acknowledge support from the JSPS KAKENHI (Grant Numbers 21H05233 and 23H02052) and World Premier International Research Center Initiative (WPI), MEXT, Japan. R

F and T H acknowledge financial support from the Oxford-ShanghaiTech collaboration project. R F, T H, and G L were supported by the Engineering and Physical Sciences Research Council under Grants EP/X015556/1 and EP/X015599/1, respectively. We thank Diamond Light Source for access to the facilities of the Materials Characterisation Laboratory. Bulk crystal synthesis and characterization (A.F.M.) were supported by the US Department of Energy, Office of Science, Basic Energy Sciences, Materials Sciences and Engineering Division.

Conflict of interest

The authors declare no competing financial interest.

ORCID iDs

Emily Heppell https://orcid.org/0000-0002-3977-4623
Ryuji Fujita https://orcid.org/0000-0001-8557-5812
Gautam Gurung https://orcid.org/0000-0001-7706-6276
Jheng-Cyuan Lin https://orcid.org/0000-0002-5085-3234
Andrew F May https://orcid.org/0000-0003-0777-8539
Michael Foerster https://orcid.org/0000-0002-4147-6668
M Waqas Khaliq https://orcid.org/0000-0002-9696-3498
Miguel Angel Niño https://orcid.org/0000-0003-3692-147X
Manuel Valvidares https://orcid.org/0000-0003-4895-8114
Javier Herrero-Martín https://orcid.org/0000-0003-1986-8128
Pierluigi Gargiani https://orcid.org/0000-0002-6649-0538
Kenji Watanabe https://orcid.org/0000-0003-3701-8119
Takashi Taniguchi https://orcid.org/0000-0002-1467-3105
Dirk Backes https://orcid.org/0000-0002-1019-3323
Gerrit van der Laan https://orcid.org/0000-0001-6852-2495
Thorsten Hesjedal https://orcid.org/0000-0001-7947-3692

References

[1] Novoselov K S, Geim A K, Morozov S V, Jiang D, Zhang Y, Dubonos S V, Grigorieva I V and Firsov A A 2004 *Science* **306** 666–9
[2] Qian X, Liu J, Fu L and Li J 2014 *Science* **346** 1344–7
[3] Yu Y *et al* 2015 *Nat. Nanotechnol.* **10** 270–6
[4] Tsen A W, Hunt B, Kim Y D, Yuan Z J, Jia S, Cava R J, Hone J, Kim P, Dean C R and Pasupathy A N 2016 *Nat. Phys.* **12** 208–12
[5] Park J G 2016 *J. Phys.: Condens. Matter* **28** 301001
[6] Burch K S, Mandrus D and Park J G 2018 *Nature* **563** 47–52
[7] Kim H H, Yang B, Patel T, Sfigakis F, Li C, Tian S, Lei H and Tsen A W 2018 *Nano Lett.* **18** 4885–90
[8] Wang X *et al* 2019 *Sci. Adv.* **5** eaaw8904
[9] Huang B *et al* 2017 *Nature* **546** 270–3
[10] Gong C *et al* 2017 *Nature* **546** 265–9
[11] Geim A K and Grigorieva I V 2013 *Nature* **499** 419–25
[12] Zhong D *et al* 2017 *Sci. Adv.* **3** e1603113
[13] Fujita R *et al* 2024 *Adv. Funct. Mater.* **34** 2400552
[14] Chen B, Yang J, Wang H D, Imai M, Ohta H, Michioka C, Yoshimura K and Fang M H 2013 *J. Phys. Soc. Jpn.* **82** 124711
[15] Fei Z *et al* 2018 *Nat. Mater.* **17** 778–82
[16] Lee J U, Lee S, Ryoo J H, Kang S, Kim T Y, Kim P, Park C H, Park J G and Cheong H 2016 *Nano Lett.* **16** 7433–8
[17] Zha H, Li W, Zhang G, Liu W, Deng L, Jiang Q, Ye M, Wu H, Chang H and Qiao S 2023 *Chin. Phys. Lett.* **40** 087501
[18] May A F, Ovchinnikov D, Zheng Q, Hermann R, Calder S, Huang B, Fei Z, Liu Y, Xu X and McGuire M A 2019 *ACS Nano* **13** 4436–42
[19] Stahl J, Shlaen E and Johrendt D 2018 *Z. Anorg. Allg. Chem.* **644** 1923–9
[20] May A F, Bridges C A and McGuire M A 2019 *Phys. Rev. Mater.* **3** 104401
[21] Yun S J, Duong D L, Ha D M, Singh K, Phan T L, Choi W, Kim Y M and Lee Y H 2020 *Adv. Sci.* **7** 1903076
[22] Wang Z, Sapkota D, Taniguchi T, Watanabe K, Mandrus D and Morpurgo A F 2018 *Nano Lett.* **18** 4303–8
[23] Gao Y, Yin Q, Wang Q, Li Z, Cai J, Zhao T, Lei H, Wang S, Zhang Y and Shen B 2020 *Adv. Mater.* **32** 2005228
[24] Park T E *et al* 2021 *Phys. Rev.* B **103** 104410
[25] Gao Y *et al* 2022 *Phys. Rev.* B **105** 014426
[26] McGuire M A 2017 *Crystals* **7** 121
[27] May A F, Du M H, Cooper V R and McGuire M A 2020 *Phys. Rev. Mater.* **4** 074008
[28] Tian C, Pan F, Xu S, Ai K, Xia T and Cheng P 2020 *Appl. Phys. Lett.* **116** 202402
[29] Chen X, Schierle E, He Y, Vranas M, Freeland J W, McChesney J L, Ramesh R, Birgeneau R J and Frano A 2022 *Phys. Rev. Mater.* **6** 094404
[30] Lu L *et al* 2024 *Nano Lett.* **24** 5984–92
[31] Chen X, Tian W, He Y, Zhang H, Werner T L, Lapidus S, Ruff J P C, Ramesh R and Birgeneau R J 2023 *Phys. Rev. Mater.* **7** 044411
[32] May A F, Yan J and McGuire M A 2020 *J. Appl. Phys.* **128** 051101
[33] Aballe L, Foerster M, Pellegrin E, Nicolas J and Ferrer S 2015 *J. Synchrotron Radiat.* **22** 745–52
[34] Foerster M, Prat J, Massana V, Gonzalez N, Fontsere A, Molas B, Matilla O, Pellegrin E and Aballe L 2016 *Ultramicroscopy* **171** 63–69
[35] Kronast F and Molina S V 2016 *J. Large-Scale Res. Facilit* **2** A90
[36] Sander A *et al* 2021 *Sci. Rep.* **11** 20788
[37] Barla A, Nicolás J, Cocco D, Valvidares S M, Herrero-Martín J, Gargiani P, Moldes J, Ruget C, Pellegrin E and Ferrer S 2016 *J. Synchrotron Rad.* **23** 1507–17
[38] van der Laan G and Figueroa A I 2014 *Coord. Chem. Rev.* **277–278** 95–129
[39] van der Laan G 1998 *Phys. Rev.* B **57** 112–5
[40] van der Laan G 1999 *J. Synchrotron Rad.* **6** 694–5
[41] Piamonteze C, Miedema P and de Groot F M F 2009 *Phys. Rev.* B **80** 184410
[42] Kresse G and Joubert D 1999 *Phys. Rev.* B **59** 1758–75
[43] Perdew J P, Burke K and Ernzerhof M 1996 *Phys. Rev. Lett.* **77** 3865–8
[44] Blöchl P E 1994 *Phys. Rev.* B **50** 17953–79
[45] Grimme S, Ehrlich S and Goerigk L 2011 *J. Comput. Chem.* **32** 1456–65
[46] Momma K and Izumi F 2008 *J. Appl. Crystal.* **41** 653–8

[47] Chen H *et al* 2023 *ACS Appl. Mater. Interfaces* **15** 3287–96

[48] Thole B T, Carra P, Sette F and van der Laan G 1992 *Phys. Rev. Lett.* **68** 1943–6

[49] Carra P, Thole B T, Altarelli M and Wang X 1993 *Phys. Rev. Lett.* **70** 694–7

[50] Chen C T, Idzerda Y U, Lin H J, Smith N V, Meigs G, Chaban E, Ho G H, Pellegrin E and Sette F 1995 *Phys. Rev. Lett.* **75** 152–5

[51] Yamagami K *et al* 2021 *Phys. Rev.* B **103** L060403

[52] Solovyev I V, Dederichs P H and Mertig I 1995 *Phys. Rev.* B **52** 13419–28

[53] Figueroa A I, Bonell F, Cuxart M G, Valvidares M, Gargiani P, van der Laan G, Mugarza A and Valenzuela S O 2020 *Phys. Rev. Lett.* **125** 226801

[54] Ohta T, Sakai K, Taniguchi H, Driesen B, Okada Y, Kobayashi K and Niimi Y 2020 *Appl. Phys. Express* **13** 043005

[55] Zhang H *et al* 2020 *Phys. Rev.* B **102** 064417

[56] Bruno P 1989 *Phys. Rev.* B **39** 865–8

[57] Dürr H A, Guo G Y, van der Laan G, Lee J, Lauhoff G and Bland J A C 1997 *Science* **277** 213–5

[58] van der Laan G 1998 *J. Phys.: Condens. Matter* **10** 3239

[59] Miura Y and Okabayashi J 2022 *J. Phys.: Cond. Matter* **34** 473001